



Tuning oxygen-containing groups of pyrene for high hydrogen peroxide production selectivity

Xiangyu Yan^{a,1}, Daohao Li^{a,1}, Lixue Zhang^b, Xiaojing Long^{a,*}, Dongjiang Yang^{a,*}

^a State Key Laboratory of Bio-fibers and Eco-textiles, Collaborative Innovation Center of Shandong Marine Biobased Fibers and Ecological textiles, Institute of Marine Biobased Materials, School of Environmental Science and Engineering, College of Materials Science and Engineering, Qingdao University, Qingdao 266071, PR China

^b College of Chemistry and Chemical Engineering, Qingdao University, Qingdao 266071, PR China

ARTICLE INFO

Keywords:

Oxygen-containing groups
Organic molecules
Charge distribution
Electrocatalysts
Hydrogen peroxide

ABSTRACT

Oxygen-containing groups (OCGs) modified carbon materials can affect the microstructure and chemical composition, which is important for oxygen reduction to hydrogen peroxide (ORHP). Thus, exploring the relationship between structure and activity of OCG-containing electrodes is of great significance. In this work, we synthesized OCGs modified pyrene-based organic molecules as electrocatalysts for ORHP. Their electrocatalytic performance are correlated with types and locations of the modified OCGs. Particularly, the **Pyr-2OMe** with better absorption of O₂ exhibits high H₂O₂ selectivity. DFT calculations reveal that the carbon atoms attached OCGs are the catalytic active sites. More importantly, the groups on one side of the molecules (**Pyr-2OMe**, **Pyr-2OH**, and **Pyr-2CO**) with large dipole moments exhibit superior catalytic activity. Thus, for the first time we find that the asymmetrically local charge redistribution of these catalysts can promote ORHP process. This work paves an alternative way to supply constructive information for understanding the structure and selectivity correlations.

1. Introduction

Hydrogen peroxide (H₂O₂) is a valuable chemical with a wide range of applications. The one-site electrochemical synthesis of H₂O₂ is a promising alternative route to traditional energy-intensive anthraquinone method [1–5]. Presently, metal-based and carbon-based materials such as single-atom-based materials and defective carbon materials have been widely investigated as electrocatalysts for H₂O₂ synthesis due to the typical two-electron oxygen reduction reaction (ORR) route [6,7]. Particularly, carbon-based materials with diverse oxygen-containing groups (OCGs), such as hydroxyl (–OH), carbonyl (–C=O) and carboxyl group (–COOH) have been extensively studied in oxygen reduction to H₂O₂ [8,9]. Generally, regulating the electronic redistribution of active sites by modification of OCGs endow enhanced selectivity and electrochemical activity. To date, the commonly used approach to develop oxygen-containing catalysts is oxidizing carbon materials, such as acetylene black, carbon nanotubes and graphene by controlling oxidation temperature. The obtained materials often contain various OCG compounds, such as –COOH, –OH, –C–O–C and –C=O, and the catalytic activity is usually improved by adjusting the

proportion of certain OCGs to weaken the adsorption of intermediates or bring synergistic effect between the OCGs in carbon-based materials [10–12]. However, due to the uncontrollable catalyst frameworks, the clear and definite active sites are usually controversial, making it difficult to clarify the relationship between activity and structure. Therefore, the development of efficient catalytic materials with definite oxygen-containing structure is of great significance for exploring the activity and mechanism of electrochemical reaction.

Conjugated organic molecules, especially organic small molecules (OSMs) with definite and tunable molecular structures, monodispersity, batch-to-batch reproducibility, have gained an inherent advantage for in-depth study of electrocatalytic mechanism and performance optimization in situ at the molecular or atomic level. After the regulation of OCGs with different electronegativity and wettability on OSMs, the redistribution of electron density and rearrangement of active groups can be efficiently induced, thus providing an ideal template for subjectively exploring the relationship of active species, electronic structures, electron transfer and the intrinsic activity/selectivity [13–19]. Among these OSMs, pyrene with a planar π conjugated pure carbon structure, endows multiple positions to vary the substitution and thus allows the

* Corresponding authors.

E-mail addresses: longxj@qdu.edu.cn (X. Long), d.yang@qdu.edu.cn (D. Yang).

¹ X.Y. Yan and D.H. Li contributed equally to this work.

regulation of type and position of OCGs [20–23], supplying a general and facile strategy of fabricating OCGs-based catalytic electrodes via a structural controllable way.

Herein, we introduced a simple synthesis strategy to prepare various oxygen group-containing pyrene-based molecules with different electronic structure by controlling their substitution location. We found that the methoxyl-containing molecule **Pyr-2OMe** with 1.0 mM cationic surfactants (CTAB) in 0.1 M KOH, shows 97.4% H₂O₂ selectivity at 0.5 V (vs. RHE), which shows the highest performance in OSMs systems. Especially, these groups on one side of the molecules (**Pyr-2CO**, **Pyr-2OH**, and **Pyr-2OMe**) with asymmetric charge redistribution exhibit larger dipole moments as well as superior selectivity and activity than those of both side counterparts (**Pyr-4CO** and **Pyr-4OMe**) with symmetric charge distribution. Density functional theory (DFT) calculations confirm that all the carbon atoms attached oxygen-containing functional groups are the catalytic active sites, especially the electron-donating methoxyl group (–OCH₃) endows its adjacent carbon atom with the lowest free energy. The small LUMO and HOMO energy level difference between oxygen and **Pyr-2OMe** can favor the absorption of the O₂, which is beneficial to the two-electron ORHP process.

2. Experimental

2.1. Chemicals and materials

All materials purchased from Aladdin, commercially available solvents and reagents were used without further purification unless stated otherwise.

2.2. Synthesis of pyrene-based molecular catalysts

Pyr-2CO: In a round bottom flask, pyrene (1 g, 5.0 mmol, 1.0 eq) and RuCl₃·xH₂O (0.10 g, 47.4 mmol, 0.1 eq) were dissolved in 20 mL of acetonitrile. NaIO₄ (4.20 g, 19.8 mmol, 4.0 eq) was dissolved in 125 mL water and carefully added to the pyrene solution. Another 20 mL of CH₂Cl₂ were added and the reaction mixture was vigorously stirred for 18 h at room temperature. The filtrate was extracted with CH₂Cl₂ (3 × 20 mL) and the combined organic phases were washed with saturated aqueous Na₂S₂O₃ and then dried over anhydrous Na₂SO₄. After removing the solvent under reduced pressure, the crude product was purified via flash chromatography (silica, CH₂Cl₂). The resultant product was obtained as a dark orange solid (500 mg, 50%). ¹H NMR (400 MHz, CDCl₃, 25 °C): δ 8.51 (dd, *J* = 7.5, 1.3 Hz, 2 H), 8.19 (dd, *J* = 8.0, 1.3 Hz, 2 H), 7.87 (s, 2 H), 7.77 (t, *J* = 7.7 Hz, 2 H). Anal. Calcd for C₁₆H₈O₂: C, 82.75; H, 3.47; O, 13.78. Found: C, 82.72; H, 3.45; O, 13.76. ICP instrument was further used to exclude the influence of Ru-element on catalytic performance.

Pyr-4CO was synthesized from pyrene and NaIO₄ (molar ratio of 1: 8) following the procedure for the synthesis of **Pyr-2CO**. The product was obtained as a brown solid (520 mg, 40%). ¹H NMR (400 MHz, CDCl₃, 25 °C): δ 8.52 (d, *J* = 7.8 Hz, 4 H), 7.73 (t, *J* = 7.7 Hz, 2 H). Anal. Calcd for C₁₆H₆O₄: C, 73.29; H, 2.31; O, 24.41. Found: C, 73.26; H, 2.29; N, 24.40.

Pyr-2OH: The obtained **Pyr-2CO** (50 mg, 1.0 eq) was added in small portions to the stirred mixture of NaHB₄ (163 mg, 10.0 eq) in ethanol (16 mL) and water (3 mL). The mixture was stirred at room temperature for 24 h, then ice-water (100 mL) is added to the solution followed with 2 M HCl. Finally, the white product can be obtained by filtration (37.5 mg, 75%). ¹H NMR (400 MHz, CDCl₃, 25 °C): δ 7.86 (d, *J* = 7.6 Hz, 2 H), 7.78 (s, 1 H), 7.66 (t, *J* = 7.6 Hz, 1 H), 5.22–5.17 (m, 2 H). ¹³C NMR (400 MHz, CDCl₃, 25 °C): δ 137.69, 130.75, 127.26, 126.93, 126.80, 126.05, 124.82, 73.29. Anal. Calcd for C₁₆H₁₂O₂: C, 81.34; H, 5.12; O, 13.54. Found: C, 81.32; H, 5.10; O, 13.53.

Pyr-2OMe: To a solution of **Pyr-2CO** (100 mg, 431 mmol) in THF (5 mL) and H₂O (5 mL) were added Tetra-*n*-butylammonium bromide (41.9 mg, 130 mmol) and Na₂S₂O₄ (226.5 mg, 1.3 mol). After 5 min, a

solution of NaOH (207.8 mg, 5.2 mmol) in H₂O (5 mL) was added to the reaction mixture followed by Me₂SO₄ (5 mL). The red-colored reaction mixture was stirred at room temperature for 1 h. The reaction mixture was extracted with ethyl acetate (30 mL). The layers were separated and the aqueous phase was extracted with ethyl acetate (20 mL). The combined ethyl acetate extracts were washed with water (30 mL) and followed by NH₃·H₂O (30 mL). The organic phase was washed by water (3 × 30 mL) followed dried over anhydrous Na₂SO₄ and the solvent was removed under reduced pressure. The product was obtained as a brown solid (85 mg, 75%). ¹H NMR (400 MHz, CDCl₃, 25 °C): δ 8.49 (dd, *J* = 7.8, 1.0 Hz, 2 H), 8.15 (dd, *J* = 7.6, 1.0 Hz, 2 H), 8.07–8.00 (m, 4 H), 4.22 (s, 6 H). Anal. Calcd for C₁₈H₁₄O₂: C, 82.42; H, 5.38; O, 12.20. Found: C, 82.40; H, 5.35; O, 12.19.

Pyr-4OMe: **Pyr-4OMe** was synthesized following the synthesis procedure of **Pyr-2OMe** by using **Pyr-4CO** as raw material. The product was obtained as a black solid (96 mg, 80%). ¹H NMR (400 MHz, CDCl₃, 25 °C): δ 8.46–8.44 (d, *J* = 7.8 Hz, 4 H), 8.07–8.03 (t, *J* = 7.8 Hz, 2 H), 4.20 (s, 12 H). Anal. Calcd for C₂₀H₁₈O₄: C, 74.52; H, 5.63; O, 19.85. Found: C, 74.52; H, 5.62; O, 19.83.

2.3. Characterization

¹H NMR spectra were measured with a Bruker AV-400 spectrometer in CDCl₃ at 25 °C. Chemical shift is reported in ppm using CHCl₃ (7.26 ppm) for ¹H NMR as an internal standard. UV–vis absorption spectra were measured with a Shimadzu UV-3600 spectrometer. ICP-OES (Avio™ 200) was used to analyze Ru-element. The morphologies and structures of the samples were characterized by using a field emission scanning electron microscopy (FESEM; Sigma 500, ZEISS, Germany). The molecular packing was investigated by powder X-ray diffraction (PXRD). PXRD data were collected on a PANalytical B.V. Empyrean powder diffractometer using a Cu K_α source (*λ* = 1.5418 Å) over the range of 2θ = 2–40° with a step size of 0.02° and 2 s per step. The contact angle is measured by the Attention Optical Contact Angle measuring instrument theta (Sweden baioulin Technology Co., Ltd). The sorption isotherm for N₂ was measured by using a BSD-PS(M) Instrument. XPS was conducted on Thermo Scientific Escalab Xi+ with an Al K_α radiation. The measurements were carried out at a pass-energy of 20.0 eV and a step size of 0.05 eV for narrow scan.

2.4. Electrochemical performance testing

LSV was conducted on a RRDE on a CHI 760 workstation, coupled to a RRDE-3A (ALS Co, Ltd.) rotator: a glassy carbon disc electrode (Ø = 4.0 mm), a Pt ring electrode (Ø inner = 5.0 mm, Ø outer = 7.0 mm), a Pt wire was used as counter electrode and Ag/AgCl as reference electrode. Catalyst was loaded onto a working electrode by drop casting 5 µL of an electrode ink at 3.0 mg mL^{−1} in a 0.5 wt% nafion solution (i.e., 0.07 mg/cm²). The measurements were typically carried out in an O₂-saturated 0.1 M KOH electrolyte at room temperature, containing 1.0 mM surfactant. LSV-RRDE was performed at an electrode rotation rate of 1600 rpm and a potential sweep rate of 10 mV s^{−1}, with a ring potential held at + 0.5 V vs Ag/AgCl (or +1.46 V vs. RHE). All potential scales were converted to RHE using: *E*_{RHE} = *E*_{Ag/AgCl} + 0.059 * pH + 0.1976. According to previous reports [24], a potential of 1.46 V (vs. RHE) can be applied on the ring of working electrode at a speed of 1600 rpm during the entire testing process. H₂O₂ selectivity of the prepared materials on the rotating ring-disk electrode was calculated based on the current of both disc and ring electrodes Eq. (1), where *I*_r is the ring current, *I*_d is the disk current and *N* is the collection efficiency (0.42 after calibration).

$$\text{H}_2\text{O}_2 (\%) = 200 * (I_r/N) / (I_r + I_d / 0.42) \quad (1)$$

$$N = 4 * I_d / (I_d + I_r / 0.42) \quad (2)$$

The H₂O₂ concentration was measured by a traditional cerium sulfate Ce(SO₄)₂ titration method based on the mechanism that a yellow

solution of Ce^{4+} would be reduced by H_2O_2 to colorless Ce^{3+} . Thus, the concentration of Ce^{4+} before and after the reaction can be measured by ultraviolet-visible spectroscopy. The wavelength used for the measurement was 316 nm. Therefore, the concentration of H_2O_2 (M) can be determined by Eq. (4): where $M_{\text{Ce}^{4+}}$ is the mole of consumed Ce^{4+} . The yellow transparent $\text{Ce}(\text{SO}_4)_2$ solution (1.00 mM) was prepared by dissolving 33.2 mg $\text{Ce}(\text{SO}_4)_2$ in 100 mL 0.50 M sulfuric acid solution. To obtain the calibration curve, H_2O_2 with known concentration was added to $\text{Ce}(\text{SO}_4)_2$ solution and measured by UV-Vis spectroscopy. Based on the linear relationship between the signal intensity and Ce^{4+} concentration (0.1–0.5 mM), the H_2O_2 concentrations of the samples could be obtained.

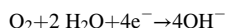
2.5. DFT calculations

The calculations were performed with the Gaussian 09 program. The structural optimizations and DFT calculations of these molecules were performed using Gaussian 09 program at the B3LYP/6–31 g (d, p) level of theory [25].

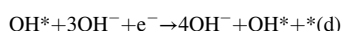
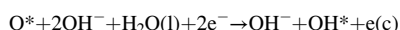
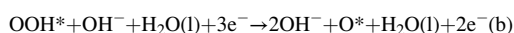
The OH^* , O^* and OOH^* intermediates were considered in the ORR. The catalytic activity of the materials was determined by the binding energies of the reaction intermediate to the active sites of the catalyst. To avoid the periodic image interaction between the two nearest neighbor unit cells (the vacuum was set to 40 Å in the z-direction), Vienna ab Initio Simulation package (VASP) was thus used as the density functional theory (DFT) calculations [26,27].

The ion–electron interactions were described by the projector plane wave (PAW) approach. Electron exchange–correlations were represented by the functional of Perdew, Burke and Ernzerhof (PBE) of generalized gradient approximation (GGA) [28]. To ensure the convergence for total energy, all calculations were performed using a plane-wave cutoff energy of 400 eV with Fermi-level smearing of 0.1 eV and Monkhorst-Pack grid ($1 \times 1 \times 1$) was used for k-point sampling. Besides, the convergence threshold of energy and forces were set to be 1×10^{-5} eV and 0.02 eV/Å, respectively.

The overall ORR in alkaline environment is [29]:



The reaction is divided into four elementary steps:



in which * implies the adsorption site.

For each step, the reaction free energy ΔG_{a} , ΔG_{b} , ΔG_{c} and ΔG_{d} is defined by following equation [30]:

$$\Delta G = \Delta E + \Delta \text{ZPE} - T\Delta S - \Delta G_{\text{U}} + \Delta G_{\text{pH}}$$

The ΔE , ΔZPE , and ΔS the different energy, zero-point energy, and entropy of the reaction, respectively. The ΔE is calculated by Density functional theory (DFT), ΔZPE , and ΔS are obtained from the values in ref [31,32].

$$\Delta G_{\text{pH}} = -kT \ln 10 * \text{pH} \quad (\text{pH}=13 \text{ is used in the ORR calculation})$$

$$\Delta G_{\text{U}} = -eU$$

in which U is the potential measured at standard conditions ($T = 298.15 \text{ K}$, $P = 1 \text{ bar}$, $\text{pH} = 13$).

The equilibrium potential ($U_{\text{ORR}}^{\text{equil}}$) for ORR is obtained by the following equation:

$$U_{\text{ORR}}^{\text{equil}} = 1.23 - kT \ln 10 * \text{pH} = 0.461 (\text{V})$$

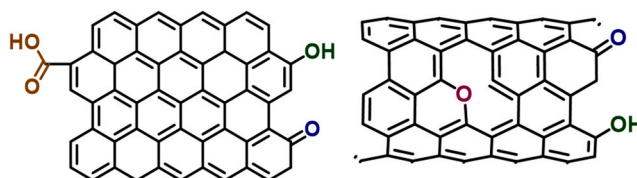
3. Results and discussion

3.1. Structure and morphology of organic molecular catalysts

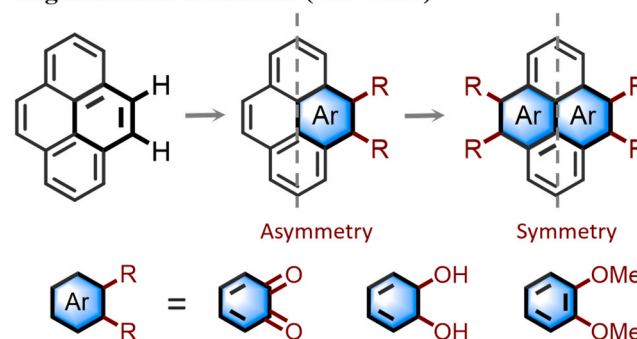
The chemical structures of pyrene-based small molecules with diverse OCGs were synthesized. Different from traditional carbon-based materials, we have developed a series of organic small molecule electrocatalysts with definite type and location of the modified oxygenated functional groups (Scheme 1 and Experimental section). Their molecular structures are confirmed by ^1H NMR and ^{13}C NMR. Fig. 1 exhibits the calculated configuration, lowest unoccupied molecular orbital (LUMO), dipole moment and electrostatic potential surface (EPS) map of the oxygen-containing molecules. Pyr-H, Pyr-2CO, Pyr-2OH and Pyr-4CO adopt nearly planar configurations (Fig. S1), while due to the steric hindrance of $-\text{OCH}_3$ group, Pyr-2OMe and Pyr-4OMe show the twisted configurations with a torsion angle of 80° between the pyrene skeleton and $-\text{OCH}_3$ group, expecting to prevent the over-aggregation of the electrode interface morphology. Dipole moment, as a measure of symmetry and charge distribution has been widely used in photocatalysis [33,34]. Thus, we have tested the dipole moment of these molecules and found that Pyr-2CO, Pyr-2OH and Pyr-2OMe with one-side oxygenated functional groups showed asymmetric charge distribution as well as enhanced dipole moments of 6.16 Debye for Pyr-2CO, 0.60 Debye for Pyr-2OH, and 0.53 Debye for Pyr-2OMe. The precisely controlled charge redistribution from varied functional groups would greatly improve their ORR performance [35–38]. More interestingly, among these asymmetric molecules, Pyr-2OMe shows more charge distribution on OCG, which is more favorable for oxygen to obtain electrons from Pyr-2OMe in ORHP process.

The morphology of the prepared organic small molecules was studied by scanning electron microscopy (SEM). All of these oxygen-containing pyrene-based catalysts showed dendritic structure and accompanied by crystallinity (Figs. 2a–2c and Fig. S2–S3). We thus measured powder X-ray diffraction (PXRD) of these catalysts to investigate the molecular stacking mode. Peaks at $2\theta = 10.52^\circ$, 11.18° , 11.80° and 10.66° for Pyr-H, Pyr-2CO, Pyr-2OH and Pyr-2OMe respectively, correspond to the (101) plane, and peaks at $2\theta = 11.14^\circ$ and 15.74° for Pyr-4CO and Pyr-4OMe correspond to the (011) and

Carbon-based materials



Organic small molecules (this work)



Scheme 1. Examples of reported oxygen-containing carbon-based materials and organic small molecular electrocatalysts (this work).

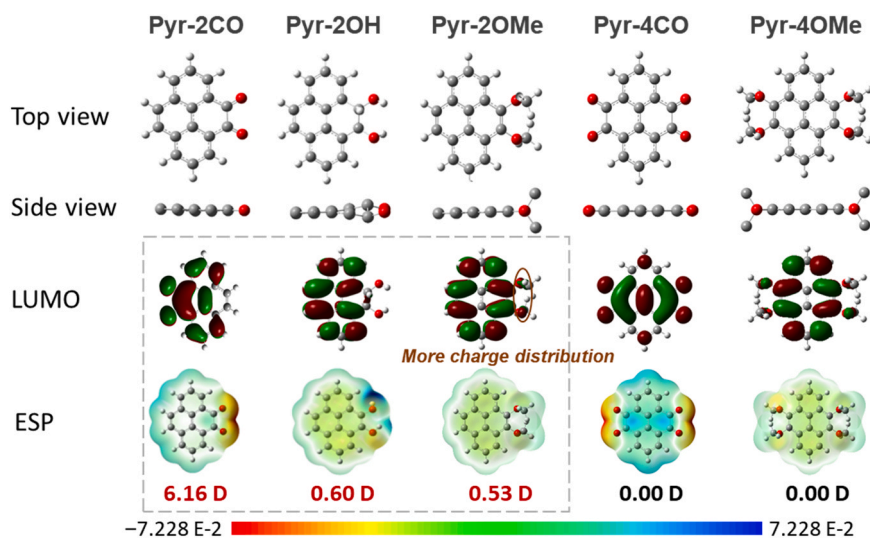


Fig. 1. The calculated molecular configuration, Kohn-Sham LUMO, electrostatic potential surface maps and dipole moments (unit: Debye (D)) of the pyrene-based molecules.

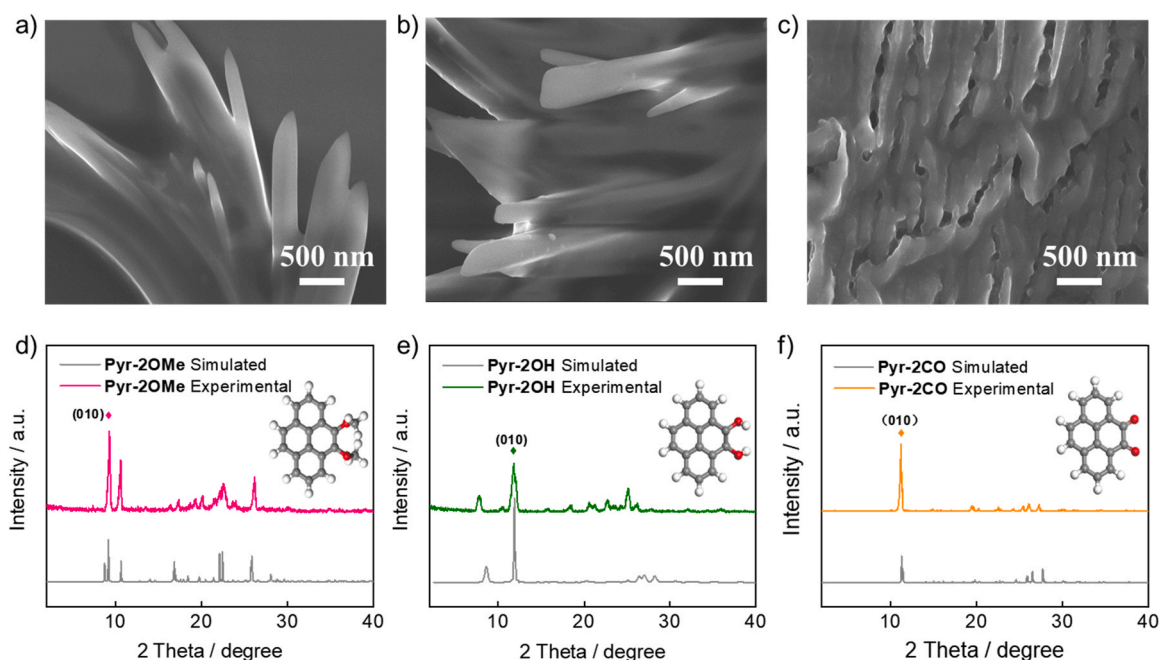


Fig. 2. The SEM of (a) Pyr-2OMe, (b) Pyr-2OH and (c) Pyr-2CO. The simulated and experimental PXRD of (d) Pyr-2OMe, (e) Pyr-2OH and (f) Pyr-2CO.

(111) planes, respectively (Figs. 2d–2f and Fig. S4). The intrinsic molecular structural characteristics and molecular stacking mode caused by OCGs will affect the hydrophilicity and hydrophobicity of electrode interface [39,40]. Therefore, we investigated the wettability characteristics of the pristine small molecules. The results demonstrate that the OCG molecules display smaller contact angles of around 65–95° than that of Pyr-H (105°) without any substituent group (Fig. S5–S6). The relatively smaller contact angles will improve the wetting ability of electrolyte to the catalysts at electrode interface. Thus, enhancing the diffusion of oxygen active species to the catalyst surface [41,42]. Fig. 3a shows the UV-Vis absorption of Pyr-2OMe in N, N-dimethylformamide (DMF) solutions. Compared to Pyr-H, the functionalized pyrene molecules Pyr-2/4CO and Pyr-2/4OMe display distinct red shifted absorption peaks, due to their enhanced conjugate lengths. However, for Pyr-2OH, the C-C single bond breaks the effective conjugation, thus the main absorption peak exhibits a blue-shifted tendency (Fig. S7). We also

performed the time-dependent DFT calculations to elucidate the UV-Vis absorption spectra. Different from high-energy band around 300 – 500 nm, the low-energy absorption band is mainly attributed to the HOMO→LUMO transition. Generally, the energy level difference between LUMO and HOMO determines the energy gap [43]. The red shift of the spectrum indicates that the HOMO level increases or the LUMO level decreases. Especially, the introduction of methoxy group can up-shift the HOMO level because of its electron donating effect. The HOMO energy levels of Pyr-2OMe with more delocalized electron distribution (Tables S1–S2) is closer to the LUMO level of oxygen. The unique electronic structures will promote efficient electron transfer from these catalysts to oxygen in ORHP [44].

Electrochemical impedance spectroscopy (EIS) and the electrochemical surface areas (ECSA) of the six pyrenyl molecules were performed in 0.1 M KOH solution by a three-electrode system. Pyr-2OMe appears the highest electrochemical surface areas (ECSA) and the

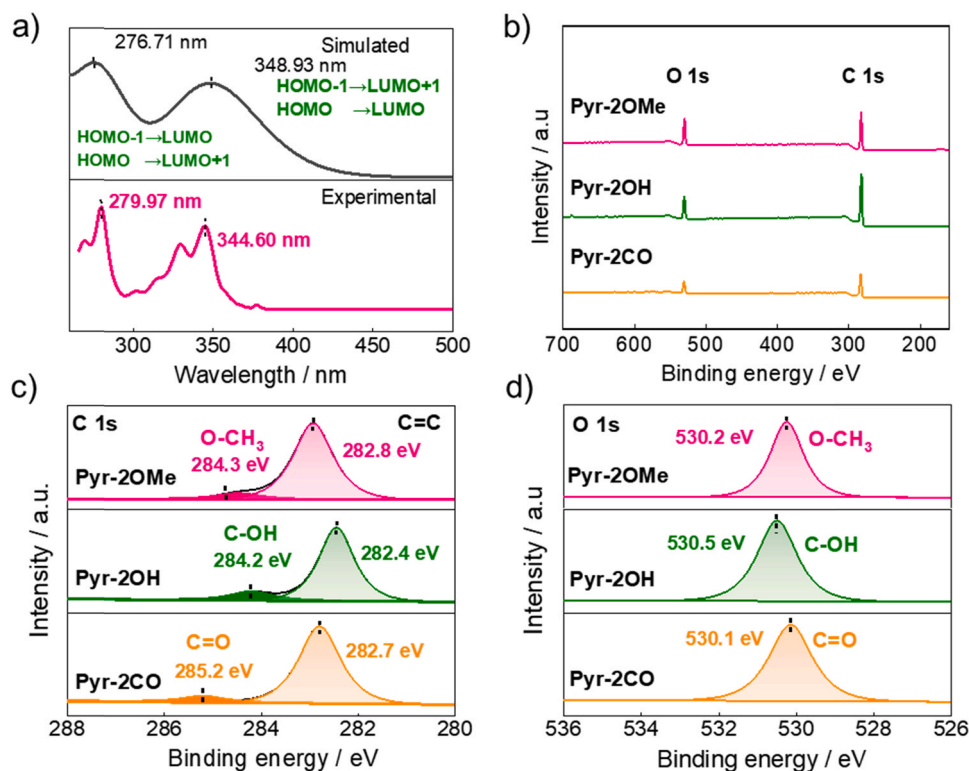


Fig. 3. (a) Simulated and experimental UV-Vis absorption of **Pyr-2OMe**. (b) XPS survey scans, (c) High-resolution C 1s spectra and (d) O 1s spectra of **Pyr-2OMe**, **Pyr-2OH** and **Pyr-2CO**.

smallest interface charge-transfer resistance (Fig. S8–S10)[45–48], indicating that the introduction of methoxyl group in pyrene plays a promoting role in ORR performance. The X-ray photoelectron spectroscopy (XPS) spectra were further conducted to identify surface chemical states and elements of the as-prepared organic molecules (Figs. 3b–3d and Fig. S11–13). Different from graphite carbon materials, the C1s peak of organic molecules is generally different. Thus, Pyr-H, Pyr-2CO, Pyr-2OH and Pyr-2OMe show varied C1s peaks of 282.6, 282.7, 282.4, and 282.8 eV,

respectively [49]. Interestingly, the C1s peaks of **Pyr-2OMe** moved to higher binding energy compared to other asymmetric **Pyr-2OH** and **Pyr-2CO** molecules. Such shifts should originate from the increased electron density around the O atoms in –OCH₃ [50], which may result in intramolecular electronic transfer due to their more charge distribution. According to previous reports, the other fitted C 1s peaks at 284.3 eV for **Pyr-2/4OMe**, 285.2 eV for **Pyr-2/4CO**, and 284.2 eV for **Pyr-2OH** are attributed to –OCH₃, C=O, and C–OH, respectively [51–53], consisting with their varied oxygen-containing molecular structures.

3.2. Electrochemical performance for ORHP

The ORHP performance of the catalysts with different oxygen-containing functional groups was evaluated by using rotating ring-disc electrode (RRDE) in an aqueous solution (O₂-saturated 0.1 M KOH electrolyte). The oxygen reduction current was detected on a disk electrode and the H₂O₂ oxidation current was measured on a Pt ring electrode at 1.46 V (vs. RHE). The collection efficiency N is 0.42 after calibration (Fig. S14). As shown in Figs. 4a–c and S15–S17, the groups on one side of the molecules **Pyr-2CO**, **Pyr-2OH** and **Pyr-2OMe** show higher ring current and activity in ORHP than those of both side counterparts (**Pyr-4CO** and **Pyr-4OMe**), as a result of exhibiting a remarkably higher H₂O₂ selectivity for **Pyr-2OMe** (88% at 0.5 V vs. RHE). The performance difference between **Pyr-2OMe** and **Pyr-4OMe** is ascribed to the uneven charge distribution and different electronegativity. This

indicates that the charge distribution regulation induced by asymmetry plays an important role in electrocatalytic activities. Cetyltrimethylammonium bromide (CTAB), as a cationic surfactant, has been proved to improve the electrocatalytic production of hydrogen peroxide in 2e–ORR process through intermolecular coulombic interaction [54, 55]. In addition to the ORHP performance of **Pyr-2OMe**, the H₂O₂ production rate was 65.0 mmol g^{–1} h^{–1} (Fig. S18). Among these small molecular catalysts, **Pyr-2OMe** with CTAB exhibits the highest H₂O₂ selectivity of 97.4% at 0.5 V and an enhanced onset potential of 0.73 V (vs. RHE), which is among the highest selectivity in the reported pyrene-based and most reported carbon catalysts (Fig. 4f and Table S3) [56–61]. The electron-transfer number also decreases to 2.04 at 0.5 V, showing obvious two electron transfer process (Figs. 4d–e and S19–S20). Similar phenomenon is also found in neutral electrolytes (Fig. S21). The stability of the **Pyr-2OMe** through a 14 h long-term stability was tested in O₂-saturated 0.1 M KOH electrolyte with 1.0 mM CTAB. The result shows that **Pyr-2OMe** is stable for a long-term H₂O₂ production, notably with a 97% activity retention over 14 h at 0 V in alkaline conditions (Fig. S22). The decomposition ratio of hydrogen peroxide under different voltages is less than 5%, which has a positive effect on the H₂O₂ production in the testing process (Fig. S23). The excellent stability of the organic molecular catalysts was further proved before and after the electrochemical reaction (Figs. S24–S30).

3.3. Density functional theory calculation

To further ensure the catalytic active site of the as-prepared materials, DFT calculations were performed on the model compounds. The reported works have revealed that the ORR activity and selectivity can be related to the binding free energy of reaction intermediate and the ORHP process [62–64]. Therefore, the catalytic activity can be determined by the corresponding energy of the crucial intermediate (OOH*).



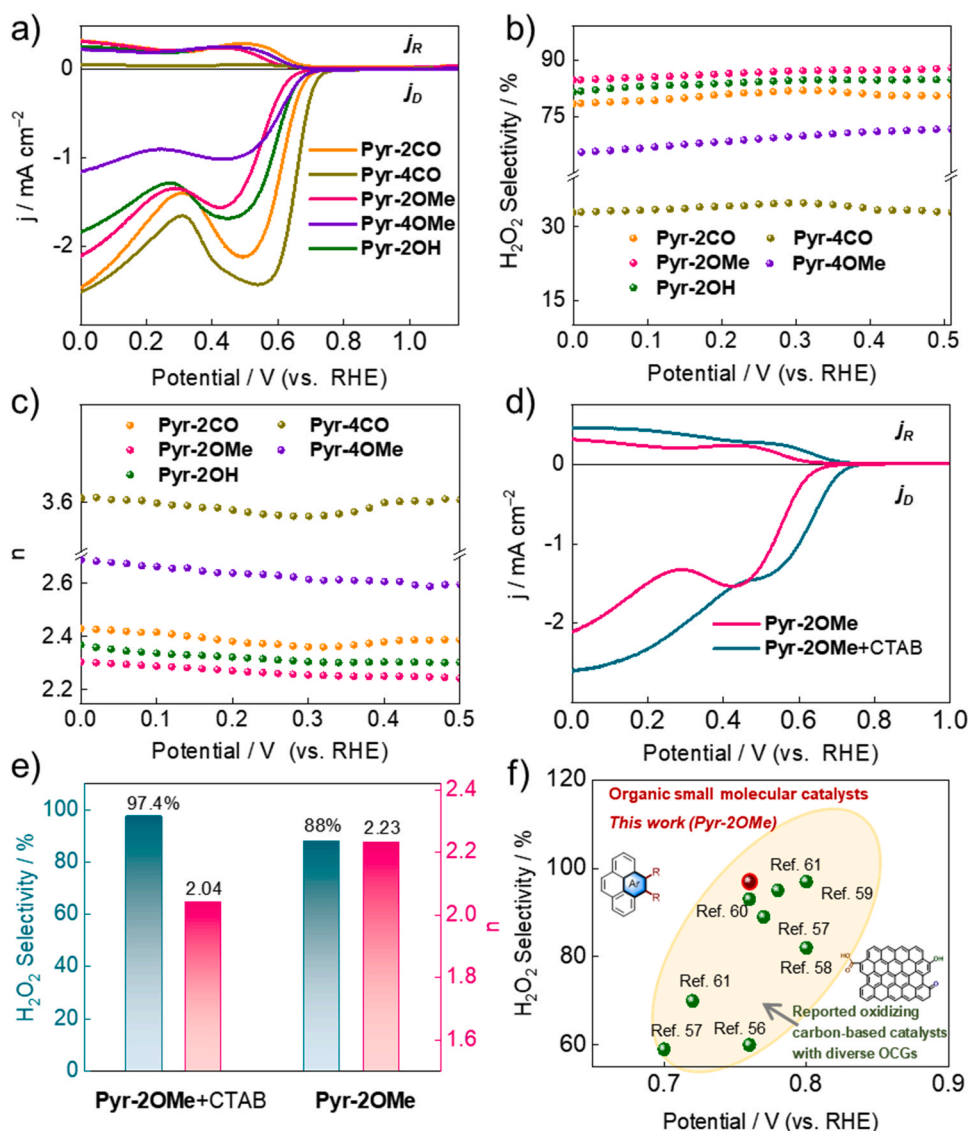
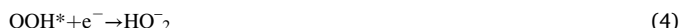


Fig. 4. (a) LSV-RRDE, (b) The corresponding H₂O₂ selectivity profiles, and (c) The electron-transfer number of the pyrene-based molecules in O₂-saturated 0.1 M KOH electrolyte. (d) LSV-RRDE and (e) The corresponding H₂O₂ selectivity profiles and electron-transfer number of Pyr-2OMe in O₂-saturated 0.1 M KOH solution with or without CTAB. (f) The onset potential and H₂O₂ selectivity distributions of reported oxidizing carbon-based catalysts and organic small molecular catalyst Pyr-2OMe (this work).



Hence, we use ΔG_{OOH^*} (binding energy of OOH*) as a descriptor and plot the activity volcano to estimate the activities of different oxygen-containing functional groups [65–67]. The maximum U_L (zero overpotential at the top of the volcano) is 0.70 V. We selected eight possible active sites to determine the overpotentials for H₂O₂ production (Fig. S31–S36). The calculated U_L as a function of ΔG_{OOH^*} for the ORHP process of these catalysts are shown Figs. 5a–5b. The structures positioned on the right side of the volcano presented the weak binding energy of OOH*, hence Eq. (1) is a limiting step. On the contrary, Eq. (2) is limiting for those located on the left side as they strongly bind OOH* [68–70]. As a result, the difference of binding strength of OOH* in oxygen-containing molecules resulted in various ORHP activities. The sites-1 on Pyr-2OMe is closer to the top of the volcano map, demonstrating the –OCH₃ group is beneficial to ORHP for weaker binding of OOH*. This finding is consistent with the above experimental results. In addition, the energy barrier of carbon atoms near oxygen (sites-1) is also lower than its counterparts (Table. S4). Density of states (DOS) shows that the oxygen-containing organic molecules endow narrower band gaps than Pyr-H around the Fermi level and better interface charge transfer, facilitating the process of the ORHP and endowing excellent

semiconductor property (Figs. 5c and S37). In order to further explore the effects of oxygen-containing functional groups on activity and selectivity, we explored the electron transfer between Pyr-2OMe and O₂. Fig. 5d shows the highest occupied molecular orbital (HOMO) orbital diagram of different molecules. It can be seen that the HOMO energy of Pyr-2OMe is –5.187 eV, which is close to the LUMO energy of oxygen, resulting in easier electron transfer from Pyr-2OMe to oxygen [71,72]. Therefore, the easier adsorption of oxygen in ORR process explain the high catalytic activity of Pyr-2OMe.

4. Conclusions

In summary, different from traditional oxidizing method to produce hydrogen peroxide, we synthesized a series of organic small molecular catalysts with definite structures and controllable active sites by modulating various oxygenated functional groups on pyrene structure. Experimental and theoretical results show that the charge is more easily transferred from Pyr-2OMe to oxygen, which is conducive to oxygen adsorption, thus endowing a highly-efficient H₂O₂ selectivity and excellent stability among these carbon-based materials. More interestingly, compared with the symmetrical Pyr-4CO and Pyr-4OMe, the asymmetric Pyr-2CO, Pyr-2OH and Pyr-2OMe show better catalytic activity due to the local charge redistribution and large dipole moments

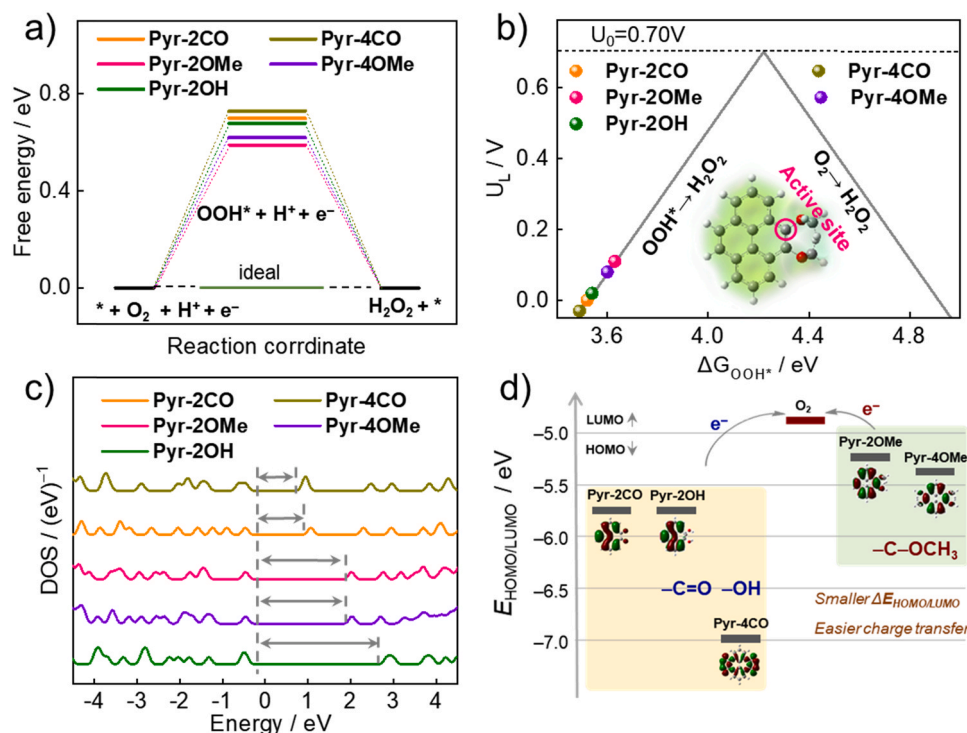


Fig. 5. (a) Free energy for ORHP of pyrene-based molecules (at site-1). (b) The calculated ORR activity volcano plot for 2e^- pathway to H_2O_2 of pyrene-based molecules, equilibrium potential of $\text{O}_2/\text{H}_2\text{O}_2$ is shown as a black dashed line. (c) DOS of pyrene-based molecules. (d) The HOMO level of pyrene-based molecules and O_2 .

caused by the asymmetric molecular structures. In this study, the effort to incorporate OCGs into organic molecules by using a simple and efficient synthesis method to study the fundamental structure–activity–selectivity relationship in ORHP process may provide a new strategy to design site-specific electrochemical electrode materials.

CRediT authorship contribution statement

Xiangyu Yan: Data curation, Formal analysis, Writing – original draft. **Daohao Li:** Formal analysis, Conceptualization, Writing – review & editing. **Lixue Zhang:** Writing – review & editing. **Xiaojing Long:** Formal analysis, Supervision, Funding acquisition, Writing – review & editing. **Dongjiang Yang:** Writing – review & editing, Supervision, Funding acquisition.

Declaration of Competing Interest

The authors declare that they have no known competing financial interests or personal relationships that could have appeared to influence the work reported in this paper.

Acknowledgments

The authors are grateful for the financial support by the National Natural Science Foundation of China (Nos. 22075157 and 21805148), Outstanding Youth of Natural Science in Shandong Province (JQ201713), the Key Research and Development Program of Shandong Province (Project 2017GSF18128), the Taishan Scholars Program (No. tsqn201909090), the Open Research Fund of State Key Laboratory of Polymer Physics and Chemistry, Changchun Institute of Applied Chemistry, Chinese Academy of Sciences

Appendix A. Supporting information

Supplementary data associated with this article can be found in the

online version at [doi:10.1016/j.apcatb.2021.120908](https://doi.org/10.1016/j.apcatb.2021.120908).

References

- [1] J.M. Campos-Martin, G. Blanco-Brieva, J. Fierro, Hydrogen peroxide synthesis: an outlook beyond the anthraquinone process, *Angew. Chem. Int. Ed.* 45 (2006) 6962–6984.
- [2] E. Brillas, I. SireS, M.A. Oturan, Electro-Fenton process and related electrochemical technologies based on Fenton's reaction chemistry, *Chem. Rev.* 109 (2009) 6570–6631.
- [3] S. Siahrostami, A. Verdager-Casadevall, M. Karamad, D. Deiana, P. Malacrida, B. Wickman, M. Escudero-Escribano, E.A. Paoli, R. Frydendal, T.W. Hansen, Corrigendum: Enabling direct H_2O_2 production through rational electrocatalyst design, *Nat. Mater.* 12 (2013) 1137–1142.
- [4] S. Yang, A. Verdager-Casadevall, L. Arnarson, L. Silvioni, V. Colic, R. Frydendal, J. Rossmeisl, I. Chorkendorff, I. Stephens, Toward the decentralized electrochemical production of H_2O_2 : a focus on the catalysis, *ACS Catal.* 8 (2018) 4064–4081.
- [5] J.K. Edwards, S.J. Freakey, R.J. Lewis, J.C. Pritchard, G.J. Hutchings, Advances in the direct synthesis of hydrogen peroxide from hydrogen and oxygen, *Catal. Today* 248 (2015) 3–9.
- [6] C. Liu, H. Li, F. Liu, J. Chen, Y. Chen, Intrinsic activity of metal centers in metal-nitrogen-carbon single-atom catalysts for hydrogen peroxide synthesis, *J. Am. Chem. Soc.* 142 (2020) 21861–21871.
- [7] K. Jiang, J. Zhao, H. Wang, Catalyst design for electrochemical oxygen reduction toward hydrogen peroxide, *Adv. Funct. Mater.* 30 (2020), 20030321.
- [8] K. Jiang, S. Back, A.J. Akey, C. Xia, H. Wang, Highly selective oxygen reduction to hydrogen peroxide on transition metal single atom coordination, *Nat. Commun.* 10 (2019) 1–12.
- [9] X. Wang, L. Nan, J.A. Webb, L.D. Pfeifferle, G.L. Haller, Effect of surface oxygen containing groups on the catalytic activity of multi-walled carbon nanotube supported Pt catalyst, *Appl. Catal. B-Environ.* 101 (2010) 21–30.
- [10] Z. Lu, G. Chen, S. Siahrostami, Z. Chen, Y. Cui, High-efficiency oxygen reduction to hydrogen peroxide catalysed by oxidized carbon materials, *Nat. Catal.* 1 (2018) 156–162.
- [11] F. Yang, X. Ma, W.B. Cai, P. Song, W. Xu, The nature of oxygen-containing groups on carbon for high-efficiency electrocatalytic CO_2 reduction reaction, *J. Am. Chem. Soc.* 141 (2019) 20451–20459.
- [12] L. Li, C. Tang, Y. Zheng, B. Xia, S. Qiao, Tailoring selectivity of electrochemical hydrogen peroxide generation by tunable pyrolic-nitrogen-carbon, *Adv. Energy Mater.* 10 (2020), 2000789.
- [13] Z.W. Guo, Y.Y. Ma, X.L. Dong, J.H. Huang, Y.G. Wang, Y.Y. Xia, An environmentally friendly and flexible aqueous zinc battery using an organic cathode, *Angew. Chem. Int. Ed.* 57 (2018) 11737–11741.

- [14] Z. Guo, J. Huang, X. Dong, Y. Xia, Y. Wang, An organic/inorganic electrode-based hydronium-ion battery, *Nat. Commun.* 11 (2020) 1–9.
- [15] K. Xu, H. Sun, T.P. Ruoko, G. Wang, R. Kroon, N.B. Kolhe, Y. Puttons, X. Liu, D. Fa Zzi, K. Shibata, Ground-state electron transfer in all-polymer donor–acceptor heterojunctions, *Nat. Mater.* 19 (2020) 738–744.
- [16] M.M. Islam, Z. Hu, Q. Wang, C. Redshaw, X. Feng, Pyrene-based aggregation-induced emission luminogens and their applications, *Mater. Chem. Front.* 3 (2019) 762–781.
- [17] F.P. Kinik, A. Ortega-Guerrero, D. Ongari, C.P. Ireland, B. Smit, Pyrene-based metal organic frameworks: from synthesis to applications, *Chem. Soc. Rev.* 50 (2021) 3143–3177.
- [18] S. Sasaki, S. Suzuki, W. Sameera, K. Igawa, K. Morokuma, G.I. Konishi, Highly twisted N, N-dialkylamines as a design strategy to tune simple aromatic hydrocarbons as steric environment-sensitive fluorophores, *J. Am. Chem. Soc.* 138 (2016) 8194–8206.
- [19] X. Long, J. Yao, F. Cheng, C. Dou, Y. Xia, Double B–N bridged bipyridine-containing polymer acceptors with enhanced electron mobility for all-polymer solar cells, *Mater. Chem. Front.* 3 (2019) 70–77.
- [20] T. M, F. Duarte, K. M, Pyrene-based materials for organic electronics, *Chem. Rev.* 111 (2011) 7260–7314.
- [21] H. Kim, K. Lee, S. Woo, Y. Jung, On the mechanism of enhanced oxygen reduction reaction in nitrogen-doped graphene nanoribbons, *Phys. Chem. Chem. Phys.* 13 (2011) 17505–17510.
- [22] L. Wang, H. Chen, Q. Daniel, L. Duan, B. Philippe, Y. Yang, H. Rensmo, L. Sun, Promoting the water oxidation catalysis by synergistic interactions between Ni(OH)₂ and carbon nanotubes, *Adv. Energy Mater.* 6 (2016), 1600516.
- [23] R. Shi, J. Guo, X. Zhang, G. Waterhouse, T. Zhang, Efficient wettability-controlled electroreduction of CO₂ to CO at Au/C interfaces, *Nat. Commun.* 11 (2020) 1–10.
- [24] X. Lu, D. Wang, K. Wu, X. Guo, W. Qi, Oxygen reduction to hydrogen peroxide on oxidized nanocarbon: Identification and quantification of active sites, *J. Colloid Interface Sci.* 573 (2020) 376–383.
- [25] M. Frisch, and G. Trucks, et al., *Gaussian 09 (Revision A.02)*, 2009.
- [26] L. Li, Y. Fang, R. Vreeker, I. Appelqvist, Reexamining the Egg-Box model in calcium–alginate gels with X-ray diffraction, *Biomacromolecules* 8 (2007) 464–468.
- [27] P. Sikorski, F. Mo, G. Skjak-Bræk, B. Stokke, Evidence for Egg-Box-compatible interactions in calcium–alginate gels from fiber X-ray diffraction, *Biomacromolecules* 8 (2007) 2098–2103.
- [28] H. Fei, J. Dong, Y. Feng, C. Allen, C. Wan, B. Voloskiy, General synthesis and definitive structural identification of Mn₄C₄ single-atom catalysts with tunable electrocatalytic activities, *Nat. Catal.* 1 (2018) 63–72.
- [29] W. Chen, J. Pei, C. He, J. Wan, H. Ren, Y. Zhu, Y. Wang, Rational design of single molybdenum atoms anchored on N-doped carbon for effective hydrogen evolution reaction, *Angew. Chem. Int. Ed.* 56 (2017) 16086–16090.
- [30] P. Yin, T. Yao, Y. Wu, L. Zheng, Y. Lin, W. Liu, H. Ju, J. Zhu, X. Hong, Z. Deng, G. Zhou, S. Wei, Y. Li, Single cobalt atoms with precise N-coordination as superior oxygen reduction reaction, *Catal., Angew. Chem. Int. Ed.* 55 (2016) 10800–10805.
- [31] G. Kresse, J. Furthmüller, Efficient iterative schemes for ab initio total-energy calculations using a plane-wave basis set, *Phys. Rev. B* 54 (1996) 11169–11186.
- [32] G. Kresse, J. Furthmüller, Efficiency of ab-initio total energy calculations for metals and semiconductors using a plane-wave basis set, *Comput. Mater. Sci.* 6 (1996) 15–50.
- [33] Q. Chen, C. Wang, Y. Li, L. Chen, Interfacial dipole in organic and perovskite solar cells, *J. Am. Chem. Soc.* 142 (2020) 18281–18292.
- [34] Z. Zhang, Y. Zhu, X. Chen, H. Zhang, J. Wang, A full-spectrum metal-free porphyrin supramolecular photocatalyst for dual functions of highly efficient hydrogen and oxygen evolution, *Adv. Mater.* (2018), 1806626.
- [35] J. Yu, B. Li, C. Zhao, J. Liu, Q. Zhang, Asymmetric air cathode design for enhanced interfacial electrocatalytic reactions in high-performance zinc–air batteries, *Adv. Mater.* 32 (2020), 1908488.
- [36] N. Fu, L. Song, J. Liu, Y. Shen, J. Siu, S. Lin, New bisoxazoline ligands enable enantioselective electrocatalytic cyano functionalization of vinylarenes, *J. Am. Chem. Soc.* 141 (2019) 14480–14485.
- [37] P. Zheng, P. Zhou, D. Wang, W. Xu, H. Wang, X. Tao, Anomalous collapses of Nares Strait ice arches leads to enhanced export of Arctic Sea ice, *Nat. Commun.* 12 (2021) 1–9.
- [38] B. Wang, W. Song, D. Li, X. Long, Y. Xia, Optimizing the oxygen reduction catalytic activity of a bipyridine-based polymer through tuning the molecular weight, *J. Mater. Chem. A* 9 (2021) 3322–3327.
- [39] Y. Liang, F. Zhao, Z. Cheng, Y. Deng, Y. Xiao, H. Cheng, P. Zhang, Y. Huang, H. Shao, L. Qu, Electric power generation via asymmetric moisturizing of graphene oxide for flexible, printable and portable electronics, *Energy Environ. Sci.* 11 (2018) 1730–1735.
- [40] X. Long, D. Li, B. Wang, Z. Jiang, W. Xu, B. Wang, D. Yang, Y. Xia, Heterocyclization strategy for construction of linear conjugated polymers: efficient metal-free electrocatalysts for oxygen reduction, *Angew. Chem. Int. Ed.* 131 (2019) 11491–11495.
- [41] K. Dong, J. Liang, Y. Wang, Z. Xu, Q. Liu, Y. Luo, T. Li, L. Li, X. Shi, A. A, Q. Li, D. Ma, X. Sun, Honeycomb carbon nanofibers: a superhydrophilic O₂-trapping electrocatalyst enables ultrahigh mass activity for the two-electron oxygen reduction reaction, *Angew. Chem. Int. Ed.* 60 (2021) 10583–10587.
- [42] Y. Sheng, S. Song, X. Wang, L. Song, C. Wang, H. Sun, X. Niu, Electrogenation of hydrogen peroxide on a novel highly effective acetylene black-PTFE cathode with PTFE film, *Electro Acta* 56 (2011) 8651–8656.
- [43] G. Zhang, M. Munoz, J.M. Etzold Bastian, Accelerating oxygen-reduction catalysts through preventing poisoning with non-reactive species by using hydrophobic ionic liquids, *Angew. Chem. Int. Ed.* 55 (2016) 2257–2261.
- [44] Y. Fang, J. Shang, D. Liu, W. Shi, X. Li, H. Ma, Design, synthesis, and application of a small molecular NIR-II fluorophore with maximal emission beyond 1200 nm, *J. Am. Chem. Soc.* 142 (2020) 15271–15275.
- [45] H. Kim, V. Bukas, H. Park, S. Park, B. M, X. Bu, Mechanisms of two-electron and four-electron electrochemical oxygen reduction reactions at nitrogen-doped reduced graphene oxide, *ACS Catal.* 10 (2020) 852–863.
- [46] H. Huang, L. Kong, M. Liu, J. He, W. Shuang, Y. Xu, X. Bu, Constructing bifunctional Co/MoC@N-C catalyst via an in-situ encapsulation strategy for efficient oxygen electrocatalysis, *J. Energy Chem.* 59 (2021) 538–546.
- [47] L. Kong, Y. Liu, H. Huang, M. Liu, W. Xu, B. Li, X. Bu, Interconnected CoS₂/NC-CNTs network as high-performance anode materials for lithium-ion batteries, *Sci. China Mater.* 64 (2021) 820–829.
- [48] S. Gao, B. Fan, J. Liu, X. Wei, R. Feng, C. Ye, X. Bu, N-doped-carbon-coated Fe₃O₄ from metal-organic framework as efficient electrocatalyst for ORR, *Nano Energy* 40 (2017) 462–470.
- [49] M. Fu, R. Lv, Y. Lei, M. Terrones, Ultralight flexible electrodes of nitrogen-doped carbon macrotube sponges for high-performance supercapacitors, *Small* 17 (2021), 2004827.
- [50] F. Yu, Z. Wang, S. Zhang, H. Ye, K. Kong, X. Gong, J. Hua, H. Tian, Molecular engineering of donor–acceptor conjugated polymer/g-C₃N₄ heterostructures for significantly enhanced hydrogen evolution under visible-light irradiation, *Adv. Funct. Mater.* 28 (2018), 1804512.
- [51] G. Greczynski, L. Hultman, Compromising science by ignorant instrument calibration—need to revisit half a century of published XPS data, *Angew. Chem. Int. Ed.* 59 (2020) 5002–5006.
- [52] M. Liu, L. Kong, X. Wang, J. He, X. Bu, Engineering bimetal synergistic electrocatalysts based on metal–organic frameworks for efficient oxygen evolution, *Small* 15 (2019), 1903410.
- [53] Z. Wei, J. Tao, C. Dz, A. Zz, H. Wei, A. Xc, The enhanced co-catalyst free photocatalytic hydrogen evolution and stability based on indenofluorene-containing donor-acceptor conjugated polymer dots/g-C₃N₄ nanosheets heterojunction, *Appl. Catal. B* 259 (2019), 118067.
- [54] K. H, W. Shi, D. Wang, J. Xu, Y. Ding, In situ electrostatic modulation of path selectivity for the oxygen reduction reaction on Fe–N doped carbon catalyst, *Chem. Mater.* 29 (2017) 4649–4653.
- [55] Y. Wang, H. Ji, W. Liu, T. Xue, C. Liu, Y. Zhang, L. Liu, Q. Wang, F. Qi, B. Xu, Novel CuCo₂O₄ composite spinel with a meso-macroporous nanosheet structure for sulfate radical formation and benzophenone-4 degradation: interface reaction, degradation pathway, and DFT calculation, *ACS Appl. Mater. Interfaces* 12 (2020) 20522–20535.
- [56] K. Wu, D. Wang, X. Zong, B. Zhang, Y. Liu, I. Gentile, D. Su, Functions in cooperation for enhanced oxygen reduction reaction: the independent roles of oxygen and nitrogen sites in metal-free nanocarbon and their functional synergy, *J. Mater. Chem. A* 5 (2017) 3239–3248.
- [57] Z. Lu, G. Chen, S. Siahrostami, Z. Chen, Y. Cui, High-efficiency oxygen reduction to hydrogen peroxide catalysed by oxidized carbon materials, *Nat. Catal.* 1 (2018) 156–162.
- [58] L. Han, Y. Sun, S. Li, C. Cheng, C. Halbig, P. Feicht, P. Strasser, S. Eigler, J. Hubner, In-plane carbon lattice-defect regulating electrochemical oxygen reduction to hydrogen peroxide production over nitrogen-doped graphene, *ACS Catal.* 9 (2019) 1283–1288.
- [59] Y. Sa, J. Kim, S. Joo, Active edge-site-rich carbon nanocatalysts with enhanced electron transfer for efficient electrochemical hydrogen peroxide production, *Angew. Chem. Int. Ed.* 58 (2019) 1100–1105.
- [60] G. Han, F. Li, W. Zou, M. Karamad, J. Baek, Building and identifying highly active oxygenated groups in carbon materials for oxygen reduction to H₂O₂, *Nat. Commun.* 11 (2020) 1–9.
- [61] K. Wu, D. Wang, X. Lu, X. Zhang, Z. Xie, Y. Liu, B. Su, J. Chen, D. Su, W. Qi, Highly selective hydrogen peroxide electrosynthesis on carbon: in situ interface engineering with surfactants, *Chem* 6 (2020) 1443–1458.
- [62] D. Li, C. Li, L. Zhang, H. Li, L. Zhu, D. Yang, Q. Fang, S. Qiu, X. Yao, Metal-free thiophene-sulfur covalent organic frameworks: precise and controllable synthesis of catalytic active sites for oxygen reduction, *J. Am. Chem. Soc.* 142 (2020) 8104–8108.
- [63] A. Kulkarni, S. Siahrostami, A. Patel, J. K, Understanding catalytic activity trends in the oxygen reduction reaction, *Chem. Soc. Rev.* 118 (2018) 2302–2312.
- [64] S. Siahrostami, A. Casadevall, M. Karamad, D. Deiana, P. Malacrida, B. Wickman, M. Escibano, E. Paoli, R. Frydendal, T. Hansen, Enabling direct H₂O₂ production through rational electrocatalyst design, *Nat. Mater.* 12 (2013) 1137–1147.
- [65] S. Chen, Z. Chen, S. Siahrostami, T. Kim, Z. Bao, Defective carbon-based materials for the electrochemical synthesis of hydrogen peroxide, *ACS Sustain. Chem. Eng.* 6 (2018) 311–317.
- [66] B. Viswanathan, Unifying the 2e[−] and 4e[−] reduction of oxygen on metal surfaces, *J. Phys. Chem. Lett.* 3 (2012) 2948–2951.
- [67] A. Casadevall, D. Deiana, M. Karamad, S. Siahrostami, I. Stephens, Trends in the electrochemical synthesis of H₂O₂: enhancing activity and selectivity by electrocatalytic site engineering, *Nano Lett.* 14 (2014) 1603–1608.
- [68] K. Jiang, S. Back, A. Akey, C. Xia, H. Wang, Double-slit photoelectron interference in strong-field ionization of the neon dimer, *Nat. Commun.* 10 (2019) 1–11.
- [69] Y. Sa, J. Kim, S. Joo, Active edge-site-rich carbon nanocatalysts with enhanced electron transfer for efficient electrochemical hydrogen peroxide production, *Angew. Chem. Int. Ed.* 58 (2019) 1100–1105.

- [70] Y. Sun, I. Sinev, W. Ju, A. Bergmann, S. Drespe, S. Kuhl, C. Spöerl, H. Schmies, H. Wang, D. Bernsmeier, Efficient electrochemical hydrogen peroxide production from molecular oxygen on nitrogen-doped mesoporous carbon catalysts, *ACS Catal.* 8 (2018) 2844–2856.
- [71] H. Wang, F.-X. Yin, N. Liu, R.-H. Kou, X.-B. He, C.-J. Sun, B.-H. Chen, D.-J. Liu, H.-Q. Yin, Engineering Fe-Fe₃C@Fe-N-C active sites and hybrid structures from dual metal-organic frameworks for oxygen reduction reaction in H₂-O₂ fuel cell and Li-O₂ battery, *Adv. Funct. Mater.* 29 (2019), 1901531.
- [72] X. Ao, W. Zhang, Z. Li, L. Lv, Y. Ruan, H.-H. Wu, W.-H. Chiang, C. Wang, M. Liu, X. C. Zeng, Unraveling the high-activity nature of Fe-N-C electrocatalysts for the oxygen reduction reaction: the extraordinary synergy between Fe-N₄ and Fe₄N, *J. Mater. Chem. A* 7 (2019) 11792–11801.